AGU PUBLICATIONS

Space Weather

RESEARCH ARTICLE
10.1002/2017SW001738

Key Points:
- Launch of FORMOSAT-5 induced large-scale circular shock acoustic waves and plasma hole in the ionosphere
- The circular waves spanned over 114–128°W in longitude and 26–39°N in latitude (~1,500 km in diameter) and lasted for ~20 min
- The circular waves are associated with the nearly vertical flight attitude of rocket due to direct orbit insertion of satellite

Correspondence to:
C. H. Lin,
charles@mail.ncku.edu.tw

Citation:
Chou, M.-Y., Shen, M.-H., Lin, C. C. H., Yue, J., Chen, C.-H., Liu, J.-Y., & Lin, J.-T. (2018). Gigantic circular shock acoustic waves in the ionosphere triggered by the launch of FORMOSAT-5 satellite. *Space Weather*, *16*, 172–184. https://doi.org/10.1002/2017SW001738

Received 30 SEP 2017
Accepted 22 JAN 2018
Accepted article online 29 JAN 2018
Published online 21 FEB 2018

Gigantic Circular Shock Acoustic Waves in the Ionosphere Triggered by the Launch of FORMOSAT-5 Satellite

Min-Yang Chou[1], Ming-Hsueh Shen[1], Charles C. H. Lin[1], Jia Yue[2,3], Chia-Hung Chen[1], Jann-Yenq Liu[4], and Jia-Ting Lin[1]

[1]Department of Earth Sciences, National Cheng Kung University, Tainan, Taiwan, [2]Atmospheric and Planetary Science, Hampton University, Hampton, VA, USA, [3]ESSIC, University of Maryland, College Park, MD, USA, [4]Institute of Space Science, National Central University, Taoyuan, Taiwan

Abstract The launch of SpaceX Falcon 9 rocket delivered Taiwan's FORMOSAT-5 satellite to orbit from Vandenberg Air Force Base in California at 18:51:00 UT on 24 August 2017. To facilitate the delivery of FORMOSAT-5 to its mission orbit altitude of ~720 km, the Falcon 9 made a steep initial ascent. During the launch, the supersonic rocket induced gigantic circular shock acoustic waves (SAWs) in total electron content (TEC) over the western United States beginning approximately 5 min after the liftoff. The circular SAWs emanated outward with ~20 min duration, horizontal phase velocities of ~629–726 m/s, horizontal wavelengths of ~390–450 km, and period of ~10.28 ± 1 min. This is the largest rocket-induced circular SAWs on record, extending approximately 114–128°W in longitude and 26–39°N in latitude (~1,500 km in diameter), and was due to the unique, nearly vertical attitude of the rocket during orbit insertion. The rocket-exhaust plume subsequently created a large-scale ionospheric plasma hole (~900 km in diameter) with 10–70% TEC depletions in comparison with the reference days. While the circular SAWs, with a relatively small amplitude of TEC fluctuations, likely did not introduce range errors into the Global Navigation Satellite Systems navigation and positioning system, the subsequent ionospheric plasma hole, on the other hand, could have caused spatial gradients in the ionospheric plasma potentially leading to a range error of ~1 m.

Plain Language Summary On 24 August 2017, a SpaceX Falcon 9 rocket departed from Vandenberg Air Force Base in California, carrying Taiwan's FORMOSAT-5 Earth observation satellite into orbit. The lightly weighted solo payload enables the rocket to fly a lofted trajectory for direct insertion at the mission altitude of 720 km. This unique nearly vertical trajectory is different from the usual satellite launches that the rockets fly over horizontal trajectory and insert satellites at 200 km altitude followed by orbit maneuvers to its mission altitudes. Consequently, the rocket launch generated a gigantic circular shock wave in the ionosphere covering a wide area four times greater than California. It is followed by ionospheric hole (plasma depletions) due to rapid chemical reactions of rocket exhaust plumes and ionospheric plasma. The ionospheric hole causing large spatial gradients could lead to ~1 m range errors into GPS navigation and positioning system. Understanding how the rocket launches affect our upper atmosphere and space environment is important as these anthropogenic space weather events are expected to increase at an enormous rate in the near future.

1. Introduction

The ionosphere consists of a great number of electrically charged particles in the Earth's upper atmosphere that can affect radio wave propagation. It is strongly influenced by disturbances like solar flares, geomagnetic storms, and solar eclipses (e.g., Afraimovich et al., 1998; Blanc & Richmond, 1980; Chimonas & Hines, 1970; Liu et al., 2004, 2013; Lin, Liu, et al., 2012; Lin, Richmond, Liu, et al., 2005; Lin, Richmond, Heelis, et al., 2005; Liu, Tsai, et al., 2006; Mannucci et al., 2005; Tanaka, 1986; Tsai & Liu, 1999). Global-scale lower atmospheric activities also contribute to significant global ionospheric variations (e.g., Immel et al., 2006; Goncharenko et al., 2010; Lin, Liu, et al., 2012; Lin, Lin, et al., 2012). Recent studies indicate that the ionosphere could also be influenced by geophysical and meteorological events on Earth, such as earthquakes, tsunamis, volcano eruptions, typhoons, and tornados (e.g., Azeem et al., 2015; Chou, Lin, Yue, Chang, et al., 2017; Chou, Lin, Yue, Tsai, et al., 2017; Dautermann et al., 2009; Liu, Chen, et al., 2011; Liu, Lin, et al., 2006; Liu & Sun, 2011; Nishioka et al., 2013; Sun et al., 2016). These natural sources can create disturbance waves that interact with the ionized and neutral particles, thus possibly introducing errors into the positioning and navigation for the Global Navigation Satellite Systems.

Over the past few decades, rapid developments in space technology have enabled human exploration beyond the Earth's orbit. With the large number of space vehicles carrying payloads into orbits, space weather effects linked to human activity have become an important issue. Since the 1960s, several studies have reported that rocket launches could cause changes to the adjacent space environment. For example, exhaust plumes generated from the shuttle or rocket launches resulted in ionospheric electron density depletions via chemical recombination process along the ascending trajectories (e.g., Booker, 1961; Furuya & Heki, 2008; Mendillo et al., 2008; Mendillo, Hawkins, & Klobuchar, 1975; Park et al., 2016). Theoretical studies and numerical model simulations on the effect of plume-released reactive molecules in the ionosphere have been conducted (Bernhardt et al., 1975; Mendillo & Forbes, 1978). The passage of rocket-triggered traveling ionospheric disturbances (TIDs) associated with the shock acoustic waves (SAWs) were investigated and simulated (Arendt, 1971; Afraimovich, Kosogorov, & Plotnikov, 2002; Calais & Minster, 1996; Donn et al., 1968; Noble, 1990; Kakinami et al., 2013; Lin et al., 2014, Lin, Chen, et al., 2017). Kakinami et al. (2013) observed the V-shape SAWs in GPS total electron content (TEC) triggered by a missile launch from North Korea on 12 December 2012 by using the dense regional GPS networks in Japan, Korea, and Taiwan. The V-shape waves had horizontal phase velocities of 1.8–2.6 km/s, which were much faster than the speed of acoustic waves reported by previous studies. Ding et al. (2014) also observed the long-distance propagation of V-shape SAWs on both sides of the rocket trajectory during the launch of the Shenzhou 10 spacecraft in China on 11 June 2013. These rocket events often generated V-shape signatures while the rockets flew horizontally in the ionosphere. Lin, Shen, et al. (2017) first reported the concentric traveling ionospheric disturbances (CTIDs) in GPS-TEC associated with the concentric gravity waves (CGWs) induced by the Falcon 9 rocket. The CGWs originated from the mesopause region after the ignition of the second-stage rocket and propagated into the ionosphere as a manifestation of CTIDs. These human-made space environment changes could introduce additional errors to the precision of positioning, navigation, reconnaissance systems and radio communication applications.

Recently, the first independently developed Earth remote sensing satellite, Formosa satellite-5 (FORMOSAT-5), of Taiwan's National Space Organization was successfully launched by the SpaceX Falcon 9 v1.2 rocket into the low Earth orbit (LEO) from the Space Launch Complex 4 East (SLC-4E) at Vandenberg Air Force Base in California on 24 August 2017. FORMOSAT-5 operates in a sun synchronous orbit at nearly 720 km altitude with 98.28° inclination angle. It carries the remote sensing instruments for providing multispectral and panchromatic imaging capabilities and the Advanced Ionospheric Probe for monitoring the ionospheric irregularities and earthquake precursors (Chen et al., 2017; Liu & Chao, 2017).

Here we apply the two-dimensional GPS-TEC observations over the continental United States (CONUS) to evaluate the ionospheric response to the launch of FORMOSAT-5. Prominent circular SAWs and an ionospheric plasma hole were observed over the western CONUS-Pacific region after the launch. Despite the frequent reports of rocket-induced V-shape SAWs, there has been no prior report of circular SAWs triggered by rocket launches. The unique orbit insertion of FORMOSAT-5 with a lofted rocket trajectory may account for the unusual circular SAWs.

This study is organized as follows: Section 2.1 presents the observations and analysis of FORMOSAT-5 induced circular waves. Section 2.2 shows the comparison of rocket-induced TIDs from previous events. Section 2.3 discusses the generation mechanism of circular SAWs. Section 2.4 briefly presents the rocket-induced ionospheric plasma hole signature. A summary is given in section 3.

2. Observations and Discussions

2.1. FORMOSAT-5 Induced Circular SAWs

According to the SpaceX Launch Report (http://www.spacex.com/sites/spacex/files/formosat5presskit.pdf), the Falcon 9 v1.2 rocket lifted off at 18:51:00 UT and deployed FORMOSAT-5 to a roughly 720 km altitude approximately 11 min after the launch. Clear ionospheric perturbations were detected from ground-based GPS networks in the U.S. after the rocket launch. We derived the vertical TEC by using the 30 s sampling GPS observational data in Receiver Independent Exchange (RINEX) format from Scripps Orbit and Permanent Array Center (http://sopac.ucsd.edu/) to study the ionospheric perturbations. The ionospheric pierce point altitude (i.e., the altitude of slant-to-vertical TEC conversion) is adjusted to 300 km, and cutoff elevation angle is set as 20° to avoid multipath errors. Then we applied a fifth-order Butterworth band-

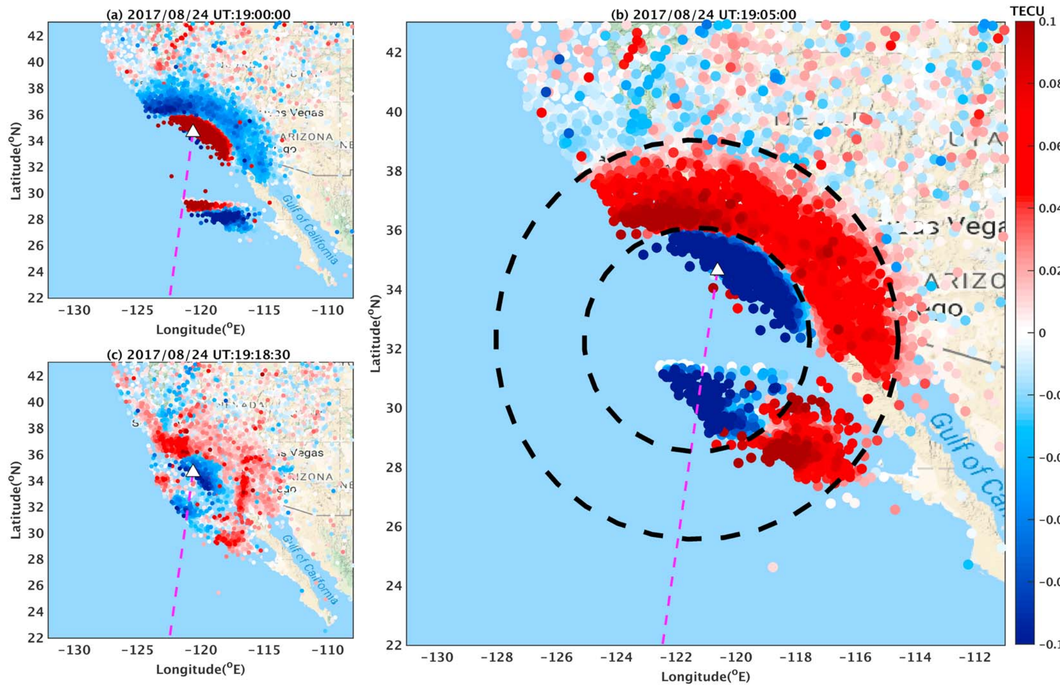

Figure 1. Two-dimensional TEC maps derived from ground-based GPS observations with the Butterworth band-pass filtering (4–15 min) indicating the concentric shock acoustic waves triggered by the launch of SpaceX Falcon 9 rocket on 24 August 2017. The Falcon 9 v1.2 rocket lifted off at 18:51:00 UT, and its trajectory and launch site are indicated by the overplotted magenta dash line and white triangle.

pass filter to extract the characteristics of SAWs associated with the rocket launch. It is common to study the ionospheric perturbation using the Butterworth band-pass filter (e.g., Bowling et al., 2013; Calais & Minster, 1995, 1996; Chen et al., 2011; Komjathy et al., 2012; Lin, Shen, et al., 2017; Yang et al., 2012). Using this type of filtering technique allows us to extract the wave perturbations within an expected range of wave periods and eliminate the long period and high amplitude TEC variations due to the daily solar activity or satellite motion. In this study, the filtered TECs with cutoff periods of 4–15 min are applied to study the TIDs corresponding to the acoustic wave. These cutoff periods are compared to those used in previous studies of rocket-induced TIDs using GPS observations (Calais & Minster, 1996; Ding et al., 2014; Lin, Shen, et al., 2017).

Figure 1 reveals the time sequence maps of Butterworth band-pass filtered TECs (4–15 min) during 19:00:00–19:18:30 UT on 24 August 2017, which shows pronounced ionospheric perturbations with a circular shape off the west coast of California. The circular waves initially appeared ~5 min after the rocket launch, and the crest and trough of circular waves quickly emanated outward with a radius of about 750 km (~1,770,000 km^2) for ~20 min. These circular waves had amplitudes exceeding 0.4 TECu (1 TECu = 10^{16} el/m^2), which corresponds to approximately 3% of the background TEC (~12 TECu), and gradually diminished by 19:18:30 UT. The origin of circular waves located right above the rocket trajectory (magenta line) suggests that the circular ripples were triggered by the rocket launch.

To better understand the characteristics of circular wave disturbances, the band-pass filtered TEC data within 120–122°W and 33–38°N are organized and plotted as a function of latitude versus time after the rocket launch. Thus, we can roughly estimate the horizontal velocities, periods, and wavelengths of circular waves, with a similar approach used in earlier studies (Chou, Lin, Yue, Chang, et al., 2017; Kotake et al., 2007). Figure 2 illustrates the various propagation velocities of circular waves that can be estimated by the slopes of slant dashed lines. The results show that the circular waves have horizontal phase velocities of ~629.15–726.02 m/s, periods of ~10.28 ± 1 min, and horizontal wavelengths of ~390–450 km. Afraimovich et al. (2002) reported the velocities of SAWs ranging from 600 to –1,100 m/s, which are close to the acoustic velocities in the upper atmosphere depending on corresponding atmospheric conditions. The horizontal

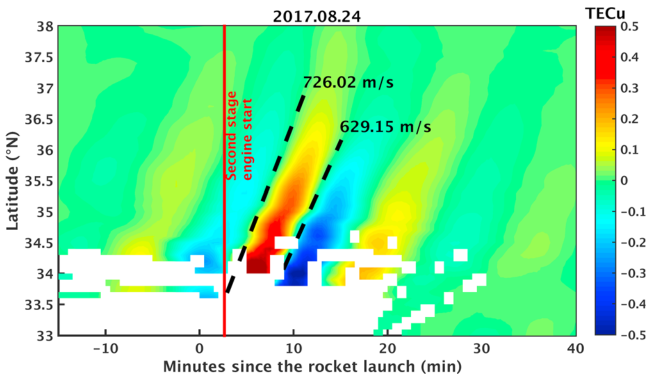

Figure 2. The time-latitude-filtered TEC (Butterworth band-pass filter) map in 120°–122°W longitudes and 33°–38°N latitudes. The red line and slant dash lines denote the second stage engine start and propagation velocities of ionospheric disturbances, respectively.

phase velocities of circular waves exceeding 600 m/s in this study are most likely related to the SAWs instead of atmospheric CGWs.

To verify the characteristics of circular waves, we calculate the theoretical acoustic velocity, acoustic cutoff, and buoyancy periods in the ideal gas (Yeh & Liu, 1974). The theoretical equation for acoustic velocity is expressed as follows:

$$C_s = \sqrt{\gamma RT/M} \tag{1}$$

where $\gamma = 7/5$ is the ratio of specific heat and $R = 8.3145$ J mol^{-1} K^{-1} is the molar gas constant. The molecular weight M and neutral temperature T are obtained from the NRLMSISE-00 empirical neutral atmosphere model (Picone et al., 2002) for the conditions on 24 August 2017 at 120°W, 35°N. Then the acoustic velocity can be computed as shown in Figure 3a. The acoustic cutoff frequency (ω_a) and buoyancy frequency (ω_b) can be expressed as follows:

$$\omega_a = \sqrt{\frac{\gamma g}{4H} + \frac{g}{T}\frac{dT}{dz}} \tag{2}$$

$$\omega_b = \sqrt{\frac{(\gamma - 1)g}{\gamma H} + \frac{g}{T}\frac{dT}{dz}} \tag{3}$$

where H and g are the scale height and gravitational acceleration. The acoustic cutoff period ($T_a = 2\pi/\omega_a$) and buoyancy period ($T_b = 2\pi/\omega_b$) have the height profiles given by Figure 3b. We note that the theoretical acoustic velocity, acoustic cutoff, and buoyancy periods at 300 km altitude are about 826.5 m/s, 13.6 min, and 15 min, respectively. The SAW velocity is essentially close to the acoustic velocity in the ionosphere. The observed wave periods (~10.28 ± 1 min) fall into the acoustic mode, but the horizontal phase velocities (~629.15–726.02 m/s) are slower than the theoretical result. The slower horizontal phase velocity might be due to the limited observational geometry of 2-D TEC map where only the horizontal component of phase velocity can be derived. If the rocket flight has a vertical component, as do the SAWs induced by it, the vertical component of the phase velocity may not be detectable. Consequently, the actual SAW velocity might be greater than that measured from the TEC maps. On the other hand, the short period implies that the impulsive circular waves are most likely related to the rocket-induced SAWs instead of atmospheric CGWs, since it is

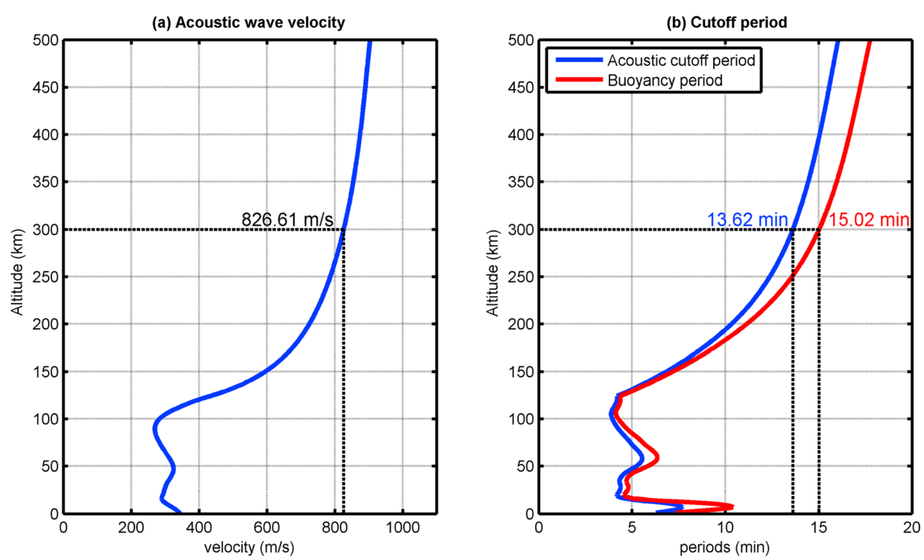

Figure 3. The vertical profile of (a) acoustic wave velocity and (b) acoustic cutoff and buoyancy periods calculated from the NRLMSISE-00 model at 120°W, 35°N on 24 August. The dash lines indicate that the acoustic wave velocity, acoustic cutoff, and buoyancy periods are 826.61 m/s, 13.62 min, and 15.02 min at 300 km altitude, respectively.

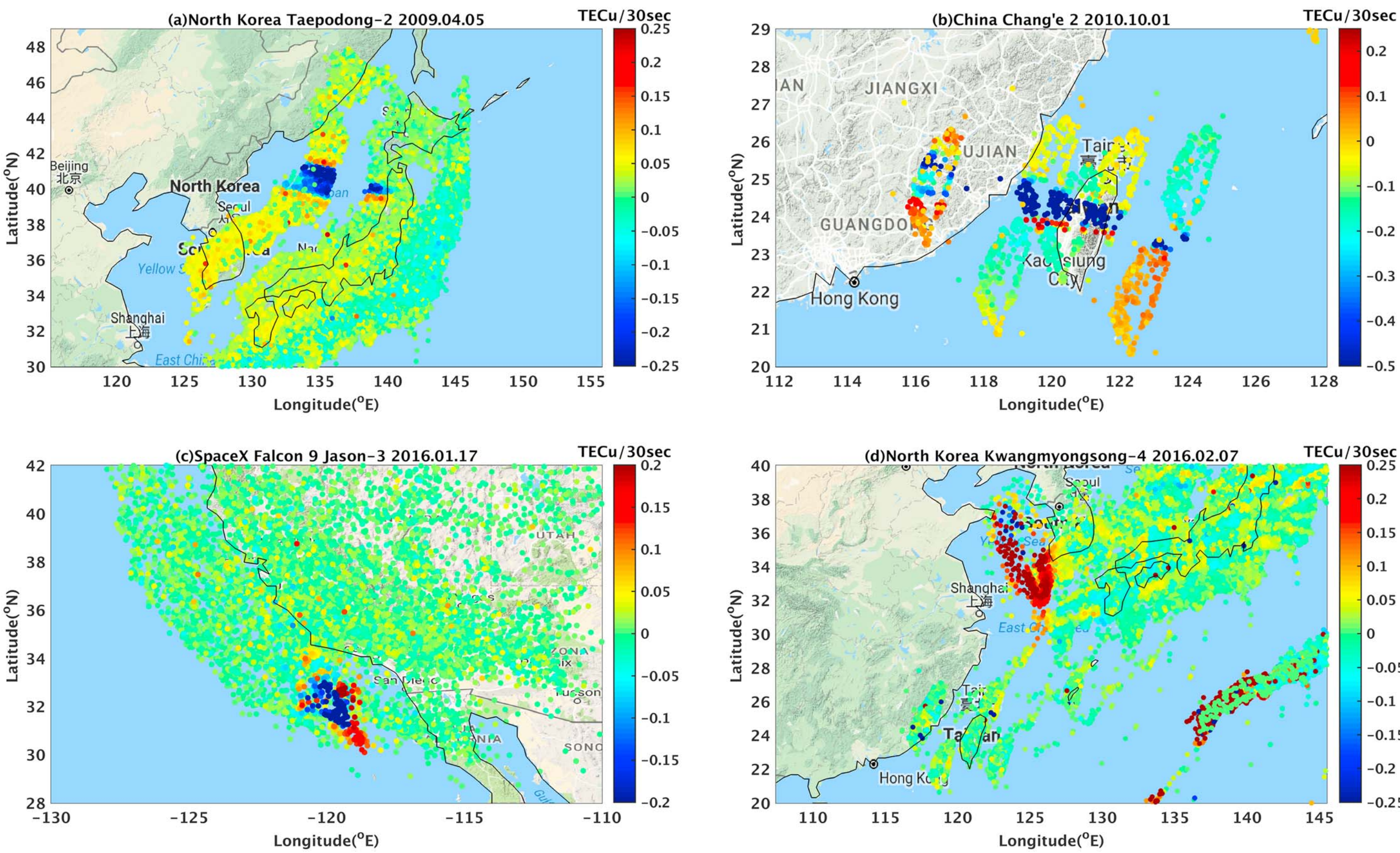

Figure 4. Snapshots of time rate change (time derivative) of TEC (rTEC) indicating the rocket-induced shock acoustic waves from (a) North Korea Taepodong-2, (b) China Chang'e 2, (c) SpaceX Falcon 9 Jason-3, and (d) North Korea Kwangmyongsong-4 missions.

impossible for a gravity wave to have period shorter than the buoyancy period. If the rocket moved faster than the sound speed, a "bow shock wave" formed by acoustic waves appears along the rocket trajectory, and the shock wave immediately decays into the acoustic mode (e.g., Ding et al., 2014; Kakinami et al., 2013; Lin et al., 2014). Similar bow shocks and stern waves were also observed during the solar eclipses (Liu, Sun, et al., 2011; Sun et al., 2018; Zhang et al., 2017).

2.2. Comparison of Rocket-Induced Ionospheric Disturbances in Other Events

2.2.1. Rocket-Induced V-Shape SAWs

To further compare the properties of rocket-induced SAWs generated in other events, a series of rocket-induced SAWs in time rate change (time derivative) of TEC (rTEC) from launches of the North Korea Taepodong-2, China Chang'e 2, SpaceX Falcon 9 JASON-3, and North Korea Kwangmyongsong-4 mission are shown in Figure 4. General information on these rocket launches are listed in Table 1 (including the launch date, time, sites, and shape of SAWs). These rocket-induced pronounced ionospheric SAWs had amplitudes of over 0.3 TECu that are comparable to the FORMOSAT-5 induced SAWs (0.4 TECu). However, they mainly resulted in the V-shape signature that is very different from the circular SAWs reported in this study.

Table 1
General Information of Rocket Launches

Mission	Launch date	Launch time	Launch site	Shape of SAWs
North Korea Taepodong-2	5 April 2009	02:30:00 UT	Musudanri	V shape
China Chang'e 2	1 October 2010	10:59:00 UT	Xichang LC-2	V shape
SpaceX Falcon 9 JASON-3	17 January 2016	18:42:18 UT	Vandenberg Air Force Base	V shape
North Korea Kwangmyongsong-4	7 February 2016	00:30:00 UT	Sohae Space Center	V shape
SpaceX Falcon 9 FORMOSAT-5	24 August 2017	18:51:00 UT	Vandenberg Air Force Base	Circular shape

Table 2
Detail Characteristics of Rocket-Induced SAWs

Mission	Amplitude (TECu)	Velocity (m/s)	Period (min)	Technique
North Korea Taepodong-2 (Lin et al., 2014)	~0.2	~831–1296	1.7–10	GPS
China Chang'e 2	~0.2–0.3	~897–904	~4–10	GPS
SpaceX Falcon 9 JASON-3 (Lin, Shen, et al., 2017)	~0.4–0.5	~808–990	~8–9	GPS
North Korea Kwangmyongsong-4 (Lin, Chen, et al., 2017)	~0.3–0.5	~873–997	6–12	GPS
SpaceX Falcon 9 FORMOSAT-5	~0.4	~629–726	~10.28	GPS

Various wave periods and horizontal phase velocities of rocket-induced SAWs are reported in previous literature by Calais and Minster (1996), Bowling et al. (2013), Ding et al. (2014), Lin et al. (2014), Lin, Shen, et al. (2017), and Lin, Chen, et al. (2017). The wave period (~10.28 min) in this study is longer than the previous events listed in Table 2, but it is still within the acoustic cutoff period shown in Figure 3b. Li et al. (1994) reported the space shuttle excited SAWs with periods of ~50–150 s at 105–110 km altitude. Ding et al. (2014) and Lin, Shen, et al. (2017) reported the rocket-induced SAWs with periods of ~9 min in the ionosphere. These studies suggest that the SAW period corresponds to the altitude reached by the rocket, since the acoustic cutoff period varies with altitude. Detailed characteristics of the rocket-induced SAWs are listed in Table 2.

Lin, Shen, et al. (2017) reported that the V-shape SAWs appeared simultaneously when the rocket reached 200 km approximately 5 min after the rocket liftoff. In this study, we observed that the circular waves emerged in the TEC maps approximately 5 min after rocket liftoff according to the SpaceX report. This coincidence indicates that the SAWs were simultaneously excited while the rocket was passing through the ionosphere.

2.2.2. Rocket-Induced Circular Waves

Lin, Shen, et al. (2017) reported remarkable patterns of V-shape SAWs and CTIDs in the ionosphere during the JASON-3 launch by the Falcon 9 v1.1 rocket from Vandenberg Air Force Base at 18:43:18 UT on 17 January 2016. The CTIDs continuously emanated outward with a number of wavefronts (crests and troughs) following the V-shape SAWs for almost 1 h with horizontal phase velocities of 241–617 m/s, periods of 10.5–12.7 min, and horizontal wavelength of ~200–400 km. The characteristics of CTIDs in Lin, Shen, et al. (2017) agree well with the gravity wave dispersion relation, suggesting the CTIDs are related to the atmospheric CGWs. We select the JASON-3 mission for comparative study since the rocket type, launch location, and local time are similar to the FORMOSAT-5 mission. Most importantly, they both triggered circular waves in the ionosphere.

At first glance, the observed circular waves in this study have some similarities to the observations of CTIDs induced by the JASON-3 launch, but they also have some differences. For example, the FORMOSAT-5 launch simultaneously produced a single impulsive circular wavefront (a single crest and a trough) instead of multiple circular wavefronts produced by the JASON-3 launch based on TEC maps. The presence of CGWs always has several simultaneous wavefronts in the middle and upper atmosphere (Miller et al., 2015). This implies that the single impulsive wave of FORMOSAT-5 launch was unlikely related to CGWs. It is more likely a SAW since the single impulsive wave pattern is similar to other previous reports of rocket-induced SAWs. Further, the circular waves induced by the FORMOSAT-5 launch lasted for ~20 min, which is much shorter than the 1 h duration of the circular waves manifested by the CGWs of the JASON-3 launch. The circular waves driven by the JASON-3 CGWs appeared ~16–40 min after the rocket liftoff, since it took tens of minutes for the CGWs to propagate from the mesosphere to the ionosphere (Lin, Shen, et al., 2017). The rapid appearance of circular waves in the ionosphere (~5 min after the Falcon 9 rocket liftoff) suggests that the CGWs were not the candidate source responsible for the waves associated with the FORMOSAT-5 launch. Furthermore, the FORMOSAT-5 induced circular waves have higher horizontal phase velocities, horizontal wavelengths, and shorter wave periods than the CTIDs induced by the JASON-3 launch.

2.3. The Generation Mechanism for Circular SAWs

The possible mechanism of FORMOSAT-5 induced circular SAWs is most likely related to the flight trajectory of rocket. We further compare the rocket's trajectory of JASON-3 with FORMOSAT-5 mission. Figure 5 shows the trajectories and velocities representing the JASON-3 (blue line) and FORMOSAT-5 (red line) launches,

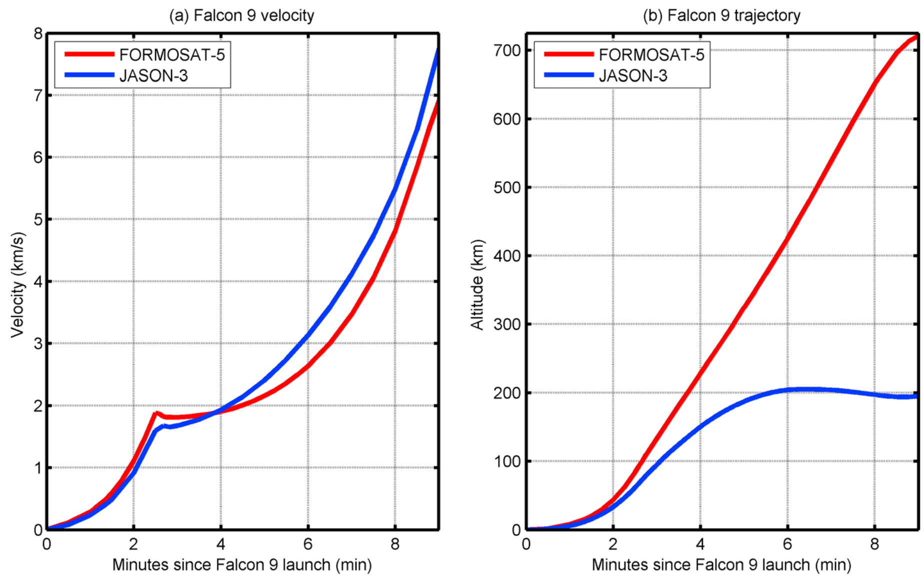

Figure 5. The Falcon 9 rocket's (a) velocities and (b) trajectories for the FORMOSAT-5 (red) and JASON-3 (blue) missions on 24 August 2017 and 17 January 2016, respectively.

respectively, based on the launch reports and videos released by SpaceX. The Falcon 9 rockets for both missions reached supersonic speed approximately ~1 min after the rocket launch and continuously accelerated to over 2 km/s above 200 km altitudes (Figure 5a). For the FORMOSAT-5 mission, the first stage fired for 2 min and 28 s accompanied with the first and second stage separation near 90 km altitude, then the second stage kept going on a single 6 min and 30 s burn, reaching about 720 km altitude nearly vertically (Figure 5b) in supersonic flight to deploy the FORMOSAT-5 satellite with 98.28° inclination angle. The first stage rocket reached the maximum altitude of 247 km, which is the highest altitude reached by a Falcon 9 booster so far. In contrast to the FORMOSAT-5 launch, the stage separation of JASON-3 launch occurred in the mesopause, and the second stage accelerated horizontally at about 200 km altitude (see Figure 5b) to reach an elliptical orbit of ~66.038° orbital inclination angle, while deployment and the circularization maneuver were implemented at apogee using satellite's onboard thrusters. There are substantial differences in the rockets' trajectories for the two missions, partly because the targeted orbits of the two missions are at different inclination and altitude. This suggests that a rocket flying vertically in the ionosphere could act as a point source to induce the circular waves, while a rocket with a horizontal flight trajectory could excite the V-shape waves along the horizontal projection of the flight trajectory as the schematic diagrams shown in Figures 6a and 6b. Furthermore, the horizontal phase velocities of circular waves and actual SAWs are functions of the cosine angle as illustrated in Figure 6c, which depicts the vertical flight of rocket-generated SAWs in the ionosphere. The blue and green arrows indicate the velocities of actual SAWs (V_{bow}) and observed circular SAWs (V_{cir}). The relationship between V_{bow} and V_{cir} is given by $V_{cir} = V_{bow}\cos(\theta)$, where θ is the included angle. This can explain the slower observed velocity compared to the theoretical acoustic velocity (826.5 m/s). For example, when the rocket reached 300 km altitude, the downrange distance from the launch site is ~180 km. Then the elevation angle of the rocket can be estimated as ~60°. The included angle should be less than or equal to 60°. If we assume the included angle to be 40°, the actual SAW velocities can be estimated as ~821–948 m/s, which are similar to previous observations of rocket-induced SAWs.

The differences between the JASON-3 and FORMOSAT-5 induced circular waves may prompt the question regarding why the FORMOSAT-5 launch did not trigger CGWs. The absence may be related to the background wind conditions that affect the upward propagation of CGWs. Yue et al. (2009) suggested that the weak background wind is a necessary condition for the CGWs propagating upward from the lower atmosphere to the middle and upper atmospheres without wind filtering. According to the Horizontal Wind Model 2014 (Drob et al., 2015), the meridional and zonal winds had maximum speeds of ~20 m/s and ~40 m/s (with altitude ranges of 25–300 km) during the FORMOSAT-5 launch. The background winds are

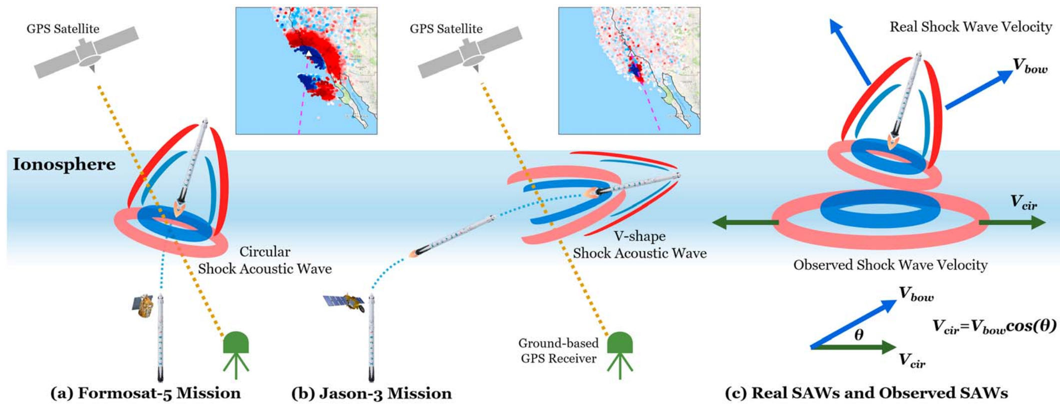

Figure 6. Cartoon illustration representing the circular and V-shape ionospheric disturbances triggered respectively by different orbit insertions of (a) FORMOSAT-5 and (b) JASON-3. The cosine angle relationship of actual SAWs (V_{bow}) and horizontal circular SAWs (V_{cir}) velocities is also shown in Figure 6c.

not expected to influence the propagation of CGWs to the ionosphere because the rocket-induced CGWs have higher horizontal phase velocities of 241–617 m/s that could reach the ionosphere from their source without much filtering (Lin, Shen, et al., 2017). Thus, we suspect that the generation of CGWs may be related to the flight trajectory of the rockets. For the launch of JASON-3, the rocket flew below 200 km altitude and gradually maneuvered from vertical to horizontal at ~200 km altitude for ~6 min after the liftoff, whereas the steep ascent of FORMOSAT-5 allowed it to stay in the middle and lower atmosphere only briefly (see Figure 5b). In fact, the atmosphere is a dissipative medium for the gravity waves especially above the mesopause region. The CGWs generated at sufficiently high altitudes are all subject to various dissipation processes such as molecular diffusion, thermal conduction, ion drag, nonlinear saturation, and other processes (Richmond, 1978; Vadas & Fritts, 2005). This implies that the rocket's dwell time below 200 km may enhance the effect of localized heating on the excitation of CGWs, and the brief stay of a rapidly moving rocket passing through the atmosphere would make the excitation of CGWs inefficient owing to the larger dissipation process at higher altitudes. In general, future investigation on the impact of flight trajectory and background atmospheric condition to the generation of CGWs and circular SAWs using theoretical modeling is still necessary.

2.4. Rocket-Induced Ionospheric Plasma Hole

Figure 7 shows the time sequence of vertical TEC maps during 18:51:00–21:30:30 UT on 24 August 2017. We select the TEC data covering 110–130°W and 30°–40°N to construct the TEC maps with spatial resolution of 1° × 1° grid (latitude-longitude). Approximately 14 min after the rocket launch, a clear TEC depletion was initially observed around 19:04:00 UT near the west edge of Vandenberg Air Force Base. Then the TEC depletions rapidly intensified and extended widely over the western CONUS-Pacific region to generate an ionospheric plasma hole with a TEC reduction of ~4 TECu. This ionospheric plasma hole extended to a wide area in diameter over 900 km (over 636,000 km^2) for ~2.5 h (~11:01–13:28 solar local time) and gradually diminished by ~21:30:00 UT. Since the large ionospheric plasma hole is localized near the Vandenberg Air Force Base and appeared after the rocket launch, we suspect that the ionospheric plasma hole can be closely associated with the rocket exhaust diffusion.

The passage of space vehicles through the upper atmosphere could result in the deposition of water vapor from exhaust plumes (Siskind et al., 2003). According to the rocket information of Falcon 9 on the SpaceX public website (http://www.spacex.com/falcon9), the first and second stages incorporate Merlin engines and aluminum-lithium alloy tanks containing liquid oxygen (LOX) and rocket-grade kerosene (RP-1) propellant. In the approximate reaction, the chemical reaction of LOX and RP-1 can produce the dominant products of carbon dioxide and water vapor (Ebbing & Gammon, 2007). When it comes to the RP-1 quasi-global combustion kinetics mechanism, the listed quasi-products are CO, H, H_2, O, OH, and O_2 (Wang, 2001). Mendillo et al. (1975) reported ionospheric TEC depletions due to the launch of NASA's Skylab. A large amount of H_2 and H_2O in the plume could result in subsequent dissociative recombination process and possible plasma loss (cf. Mendillo et al., 2008).

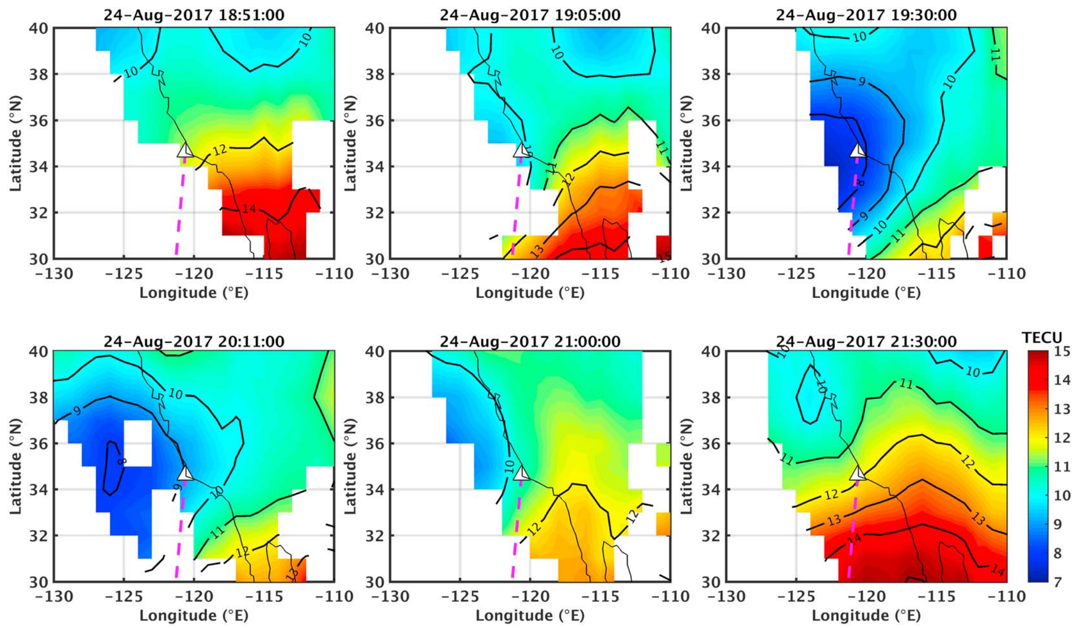

Figure 7. Two-dimensional maps of total electron content derived from ground-based GPS observations during 18:51:00–21:30:00 UT showing a large ionospheric plasma hole after the launch of SpaceX Falcon 9 rocket on 24 August 2017. The overplotted magenta dash line and white triangle indicate the rocket's trajectory and launch site.

The rocket-induced TEC depletions often display a band structure along the rocket's trajectory (Lin et al., 2014; Mendillo et al., 2008; Nakashima & Heki, 2014; Ozeki & Heki, 2010). However, in this study, the ionospheric plasma hole displays a circular shape off the west coast of the United States. It is possible for the vertical flight of rocket to act as point source to generate a circular hole. We note that the ionospheric plasma hole has greater TEC depletions on the west side of the rocket's trajectory. The rocket exhaust plumes can move with the neutral wind and make an asymmetric TEC depletion signature along the trajectory (Choi & Kil, 2017). According to the Horizontal Wind Model 2014, northwestward background winds with velocities of 40–50 m/s (at 300 km altitude) along the rocket's trajectory may spread the water vapor of plumes and account for the westward shift of plasma hole.

We further calculate the GPS TEC from 16 to 31 August 2017 as reference days to estimate percentage changes due to the rocket launch by subtracting reference days TEC from that of the launch date. The GPS TEC was organized around 120–125°W (longitude) and 30°–40°N (latitude) to acquire better data coverage. Then percentage changes between the TEC during 16–31 August (TEC_N) and 24 August (TEC'), defined as $\frac{TEC' - TEC_N}{TEC_N}$, can be determined. Figure 8 shows that the latitude-time-TEC percentage deviation maps have prominent TEC depletions of ~10–70% during 19:00–22:00 UT on the launch day in comparison to the reference days. The peak TEC depletions appeared at ~33–35°N near the launch site after 19:00 UT. This implies that the FORMOSAT-5 induced ionospheric plasma hole was most likely made by the second stage rocket in the lower ionosphere. Kakinami et al. (2013) suggested that the TEC depletion was not strong enough to be observed in the topside ionosphere while the rocket passed through the ionospheric height above 391 km from North Korea on 12 December 2012. Nakashima and Heki (2014) further applied the Russian Global Navigation Satellite System (GLONASS; Global'naya Navigatsionnaya Sputnikovaya Sistema) TEC to study the same case; clear TEC depletions were observed over the Yellow Sea at 280 km altitude.

We can estimate the dissipation time of ionospheric plasma hole based on the continuity equation of TEC described by Mendillo et al. (1975):

$$\frac{dN_T}{dt} = q - \beta_{eff} N_T + M \tag{4}$$

where N_T, q, β_{eff}, and M indicate the TEC, TEC production rate, effective loss coefficient, and divergence of plasma motion, respectively. The hourly TEC variation and background TEC (N_T) at 34–36°N are about 1

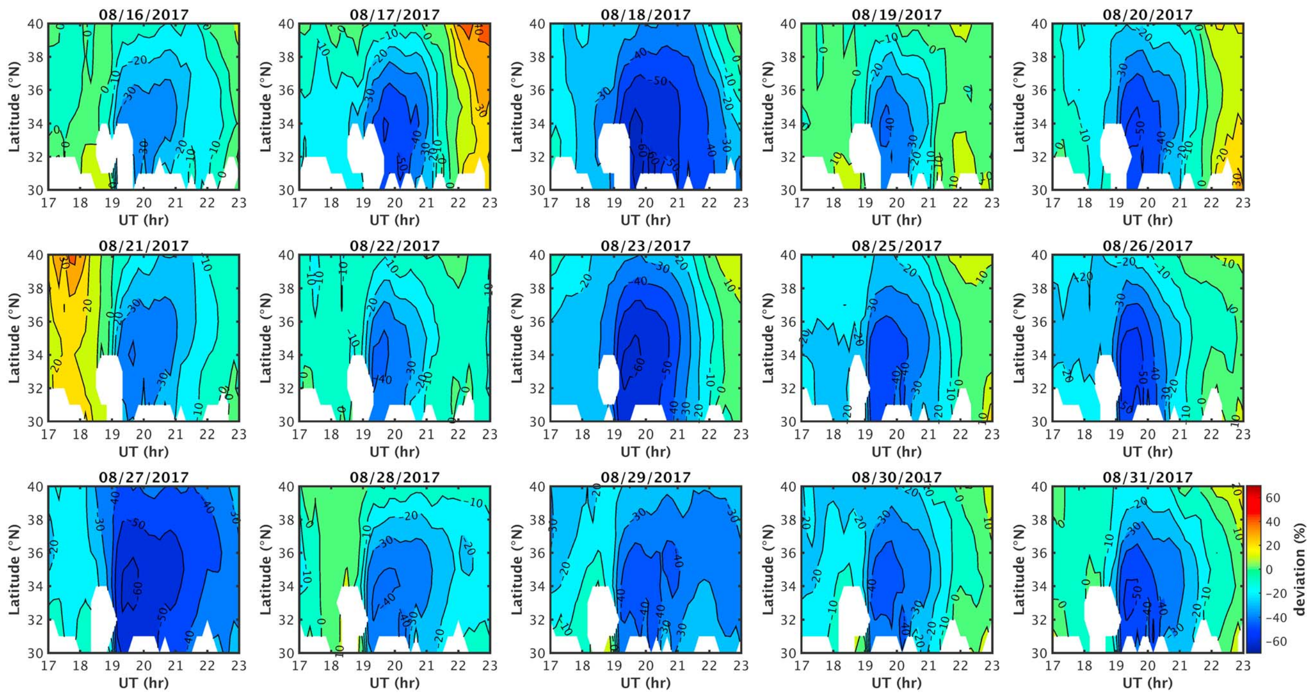

Figure 8. The latitude-UT-TEC percentage deviation maps within 120–125°W (longitude) and 30°–40°N (latitude) during 16–31 August 2017. Each tile shows TEC deviation values relative to 24 August 2017. Clear TEC depletions occurred at ~19:00–22:00 UT after the rocket launch.

TECu and 12 TECu from 18:00 to 19:00 UT before the rocket launch. Then the time rate change of TEC, $\frac{dN_T}{dt} = \frac{1\ \text{TECu}}{3{,}600\ s}$, β_{eff} given by Mendillo et al. (1975) is $1.98 \times 10^{-5}\ s^{-1}$. Assuming $q + M$ will be constant before and after the rocket launch, plugging each constant into equation (4), the q + M can be evaluated as follows:

$$q + M = \frac{dN_T}{dt} + \beta_{\text{eff}} N_T \simeq \frac{1\ (\text{TECu})}{3{,}600\ (\text{s})} + \left(1.98 \times 10^{-5} \left(\text{s}^{-1}\right)\right) \times 12\ (\text{TECu}) \simeq 5 \times 10^{-4}\ (\text{TECu/s}) \tag{5}$$

After the rocket launch, the continuity equation can be revised as follows:

$$\frac{dN_T}{dt} = q + M - \beta N_T \tag{6}$$

where β indicates the enhanced loss coefficient due to the constituents of rocket plume. Note that the loss coefficient β is determined by the diffusion time, distance from the source, and concentration for the molecular of exhaust plume. The radial distance from the rocket's trajectory to the peak TEC depletion are about 500–700 km (Figure 7d). We assume $\beta = 3 \times 10^{-5}\ s^{-1}$ for the conditions of rocket exhaust released within 700 km distance and 2 h after liftoff according to Figure 8c of Mendillo et al. (1975). The background TECs inside and outside of the ionospheric plasma hole from Figure 7 are estimated about 7 TECu and 10.5 TECu, respectively. Then the N_T = 7 TECu and ΔN_T = 10.5 − 7 = 3.5 TECu. The dissipation time for the ionospheric plasma hole can be estimated as follows:

$$\Delta t \approx \frac{\Delta N_T}{q + M - \beta N_T} \approx \frac{3.5\ (\text{TECu})}{5 \times 10^{-4} - 3 \times 10^{-5} \times 7\ \left(\frac{\text{TECu}}{\text{s}}\right)} \approx 3.35\ \text{h} \tag{7}$$

The theoretical dissipation time for the ionospheric plasma hole is essentially consistent with the observational result of ~2.5–3 h from Figures 7 and 8 suggesting that the TEC depletions are exactly related to the rocket exhaust.

3. Summary

We present the first observation of circular SAWs triggered by the launch of SpaceX Falcon 9 rocket carrying FORMOSAT-5 satellite on 24 August 2017. The Falcon 9 rocket reached 300 km altitude approximately 5 min after the rocket liftoff and simultaneously induced pronounced circular SAWs with horizontal phase velocities of ~629.15–726.02 m/s, horizontal wavelengths of ~390–450 km, and periods of ~10.28 ± 1 min. The circular SAWs, extending over 1,770,000 km^2 in area, over the western CONUS-Pacific region are the largest rocket-induced SAWs on record, to our knowledge. The SAWs displaying the circular shape instead of V-shape are most likely attributed to the nearly vertical flight of rocket that acts as a point source to generate the circular SAWs. These circular SAWs with amplitudes exceeding 0.4 TECu correspond to approximately 3% of the background TEC (~12 TECu), which has little impact on the navigation accuracy of GPS. Following the circular SAWs, the rocket exhaust plumes generated a large-scale circular ionospheric plasma hole via chemical reactions with a TEC reduction of ~4 TECu and diameter over 900 km (636,000 km^2). The ionospheric plasma hole appeared ~13 min after the rocket launch and caused ~10–70% of TEC depletions in comparison with the reference days. The greater TEC depletions of ionospheric plasma hole on the northwest side of the rocket's trajectory may be related to the northwestward wind. The theoretical dissipation time agrees well with the recovery time of ionospheric plasma hole of ~2.5–3 h (~11:01–13:58 solar local time). This suggests that large amounts of the second-stage rocket exhaust plumes were released into the ionosphere producing electron density depletions via subsequent plasma recombination process. The resulting plasma gradients in the ionosphere should impose ~1 m range error on GPS navigation.

Acknowledgments
This study is supported by the Ministry of Science and Technology, Taiwan, under MOST 106-2111-M-006-001 and 106-2119-M-006-025 and the National Space Organization under NSPO-S-105120 and NSPO-S-106012. The authors acknowledge Scripps Orbit and Permanent Array Center (SOPAC) for providing the GPS RINEX data (ftp://garner.ucsd.edu). We are grateful to the constructed suggestions given by the two anonymous reviewers and Editor.

References

Afraimovich, E. L., Kosogorov, E. A., & Plotnikov, A. V. (2002). Shock–acoustic waves generated during rocket launches and earthquakes. *Cosmic Research*, *40*(3), 241–254. https://doi.org/10.1023/A:1015925020387

Afraimovich, E. L., Palamartchouk, K. S., Perevalova, N. P., & Chernukhov, V. V. (1998). Ionospheric effects of the solar eclipse of March 9 (1997), as deduced from GPS data. *Geophysical Research Letters*, *25*(4), 465–468. https://doi.org/10.1029/98GL00186

Arendt, P. R. (1971). Ionospheric undulations following Apollo 14 launching. *Nature*, *231*(438), 1971.

Azeem, I., Yue, J., Hoffmann, L., Miller, S. D., Straka, W. C., & Crowley, G. (2015). Multisensor profiling of a concentric gravity wave event propagating from the troposphere to the ionosphere. *Geophysical Research Letters*, *42*, 7874–7880. https://doi.org/10.1002/2015GL065903

Bernhardt, P. A., Park, C. G., & Banks, P. M. (1975). Depletion of the F_2 region ionosphere and the protonosphere by the release of molecular hydrogen. *Geophysical Research Letters*, *2*(8), 341–344. https://doi.org/10.1029/GL002i008p00341

Blanc, M., & Richmond, A. D. (1980). The ionospheric disturbance dynamo. *Journal of Geophysical Research*, *85*(A4), 1669–1686. https://doi.org/10.1029/JA085iA04p01669

Booker, H. G. (1961). A local reduction of *F*-region ionization due to missile transit. *Journal of Geophysical Research*, *66*(4), 1073–1079. https://doi.org/10.1029/JZ066i004p01073

Bowling, T., Calais, E., & Haase, J. S. (2013). Detection and modelling of the ionospheric perturbation caused by a space shuttle launch using a network of ground-based Global Positioning System stations. *Geophysical Journal International*, *192*(3), 1324–1331. https://doi.org/10.1093/gji/ggs101

Calais, E., & Minster, J. B. (1995). GPS detection of ionospheric perturbations following the January 17, 1994, Northridge earthquake. *Geophysical Research Letters*, *22*(9), 1045–1048. https://doi.org/10.1029/95GL00168

Calais, E., & Minster, J. N. (1996). GPS detection of ionospheric perturbations following a space shuttle ascent. *Geophysical Research Letters*, *23*(15), 1897–1900. https://doi.org/10.1029/96GL01256

Chen, C. H., Lin, C. C. H., Liu, J. Y., Matsuo, T., & Chen, W. H. (2017). The impact of FORMOSAT-5/AIP observations on the ionospheric space weather. *Terrestrial, Atmospheric and Oceanic Sciences*, *28*(2), 129–137. https://doi.org/10.3319/TAO.2016.09.30.01(EOF5)

Chen, C. H., Saito, A., Lin, C. H., Liu, J. Y., Tsai, H. F., Tsugawa, T., et al. (2011). Long-distance propagation of ionospheric disturbance generated by the 2011 off the Pacific coast of Tohoku Earthquake. *Earth, Planets and Space*, *63*, 881–884. https://doi.org/10.5047/eps.2011.06.026

Chimonas, G., & Hines, C. O. (1970). Atmospheric gravity waves induced by a solar eclipse. *Journal of Geophysical Research*, *75*(4), 875. https://doi.org/10.1029/JA075i004p00875

Choi, B. K., & Kil, H. (2017). Large ionospheric TEC depletion induced by the 2016 North Korea rocket. *Advances in Space Research*, *59*(2), 532–541.

Chou, M. Y., Lin, C. C. H., Yue, J., Tsai, H. F., Sun, Y. Y., Liu, J. Y., & Chen, C. H. (2017). Concentric traveling ionosphere disturbances triggered by super typhoon Meranti (2016). *Geophysical Research Letters*, *44*, 1219–1226. https://doi.org/10.1002/2016GL072205

Chou, M. Y., Lin, C. H., Yue, J., Chang, L. C., Tsai, H. F., & Chen, C. H. (2017). Medium-scale traveling ionospheric disturbances triggered by super typhoon Nepartak (2016). *Geophysical Research Letters*, *44*, 7569–7577. https://doi.org/10.1002/2017GL073961

Dautermann, T., Calais, E., & Mattioli, G. (2009). Global Positioning System detection and energy estimation of the ionospheric wave caused by the 13 July 2003 explosion of the Soufriere Hills Volcano, Montserrat. *Journal of Geophysical Research*, *114*, B02202. https://doi.org/10.1029/2008JB005722

Ding, F., Wan, W., Mao, T., Wang, M., Ning, B., Zhao, B., & Xiong, B. (2014). Ionospheric response to the shock and acoustic waves excited by the launch of the Shenzhou 10 spacecraft. *Geophysical Research Letters*, *41*, 3351–3358. https://doi.org/10.1002/2014GL060107

Donn, W. L., Posmentier, E., Fehr, U., & Balachandran, N. K. (1968). Infrasound at long range from Saturn V, 1967. *Science*, *162*(3858), 1116–1120. https://doi.org/10.1126/science.162.3858.1116

Drob, D. P., Emmert, J. T., Meriwether, J. W., Makela, J. J., Doornbos, E., Conde, M., et al. (2015). An update to the horizontal wind model (HWM): The quiet time thermosphere. *Earth Space Science*, *2*(7), 301–319. https://doi.org/10.1002/2014EA000089

Ebbing, D. and Gammon SD 2007. General chemistry. Cengage Learning, Boston, MA. pp. 251. ISBN 978-1-111-80895-2.

Furuya, T., & Heki, K. (2008). Ionospheric hole behind an ascending rocket observed with a dense GPS array. *Earth, Planets and Space*, *60*(3), 235–239. https://doi.org/10.1186/BF03352786

Goncharenko, L. P., Chau, J. L., Liu, H.-L., & Coster, A. J. (2010). Unexpected connections between the stratosphere and ionosphere. *Geophysical Research Letters*, *37*, L10101. https://doi.org/10.1029/2010GL043125

Immel, T. J., Sagawa, E., England, S. L., Henderson, S. B., Hagan, M. E., Mende, S. B., et al. (2006). Control of equatorial ionospheric morphology by atmospheric tides. *Geophysical Research Letters*, *33*, L15108. https://doi.org/10.1029/2006GL026161

Kakinami, Y., Yamamoto, M., Chen, C.-H., Watanabe, S., Lin, C., Liu, J.-Y., & Habu, H. (2013). Ionospheric disturbances induced by a missile launched from North Korea on 12 December 2012. *Journal of Geophysical Research: Space Physics*, *118*, 5184–5189. https://doi.org/10.1002/jgra.50508

Komjathy, A., Galvan, D. A., Stephens, P., Butala, M. D., Akopian, V., Wilson, B. D., et al. (2012). Detecting ionospheric TEC perturbations caused by natural hazards using a global network of GPS receivers: The Tohoku case study. *Earth, Planets and Space*, *64*, 1–8.

Kotake, N., Otsuka, Y., Ogawa, T., Tsugawa, T., & Saito, A. (2007). Statistical study of medium-scale traveling ionospheric disturbances observed with the GPS networks in southern California. *Earth, Planets and Space*, *59*, 95–102. https://doi.org/10.1186/BF03352681

Li, Y. Q., Jacobson, A. R., Carlos, R. C., Massey, R. S., Taranenko, Y. N., & Wu, G. (1994). The blast wave of the shuttle plume at ionospheric heights. *Geophysical Research Letters*, *21*(24), 2737–2740. https://doi.org/10.1029/94GL02548

Lin, C. H., Chen, C.-H., Matsumura, M., Lin, J.-T., & Kakinami, Y. (2017). Observation and simulation of the ionosphere disturbance waves triggered by rocket exhausts. *Journal of Geophysical Research: Space Physics*, *122*, 8868–8882. https://doi.org/10.1002/2017JA023951

Lin, C. H., Lin, J. T., Chen, C. H., Liu, J. Y., Sun, Y. Y., Kakinami, Y., et al. (2014). Ionospheric shock waves triggered by rockets. *Annales de Geophysique*, *32*(9), 1145–1152. https://doi.org/10.5194/angeo-32-1145-2014

Lin, C. H., Richmond, A. D., Heelis, R. A., Bailey, G. J., Lu, G., Liu, J. Y., et al. (2005). Theoretical study of the low- and midlatitude ionospheric electron density enhancement during the October 2003 superstorm: Relative importance of the neutral wind and the electric field. *Journal of Geophysical Research*, *110*, A12312. https://doi.org/10.1029/2005JA011304

Lin, C. H., Richmond, A. D., Liu, J. Y., Yeh, H. C., Paxton, L. J., Lu, G., et al. (2005). Large-scale variations of the low-latitude ionosphere during the October–November 2003 superstorm: Observational results. *Journal of Geophysical Research*, *110*. A09S28. https://doi.org/10.1029/2004JA010900

Lin, C. H., Shen, M.-H., Chou, M.-Y., Chen, C.-H., Yue, J., Chen, P.-C., & Matsumura, M. (2017). Concentric traveling ionospheric disturbances triggered by the launch of a SpaceX Falcon 9 rocket. *Geophysical Research Letters*, *44*, 7578–7586. https://doi.org/10.1002/2017GL074192

Lin, C. Y., Liu, J. Y., Lin, C. H., Sun, Y. Y., Araujo-Pradere, E. A., & Kakinami, Y. (2012). Using the IRI, the MAGIC model, and the co-located ground-based GPS receivers to study ionospheric solar eclipse and storm signatures on July 22, 2009. *Earth, Planets and Space*, *64*(6), 513–520. https://doi.org/10.5047/eps.2011.08.016

Lin, J. T., Lin, C. H., Chang, L. C., Huang, H. H., Liu, J. Y., Chen, A. B., et al. (2012). Observational evidence of ionospheric migrating tide modification during the 2009 stratospheric sudden warming. *Geophysical Research Letters*, *39*, L02101. https://doi.org/10.1029/2011GL050248

Liu, J. Y., & Chao, C. K. (2017). An observing system simulation experiment for FORMOSAT-5/AIP detecting seismo-ionospheric precursors. *Terrestrial, Atmospheric and Oceanic Sciences*, *28*(2), 117–127. https://doi.org/10.3319/TAO.2016.07.18.01(EOF5)

Liu, J. Y., & Sun, Y. Y. (2011). Seismo-traveling ionospheric disturbances of ionograms observed during the 2011 Mw9.0 Tohoku Earthquake. *Earth Planets Space*, *63*, 897–902.

Liu, J.-Y., Chen, C.-H., Lin, C.-H., Tsai, H.-F., Chen, C.-H., & Kamogawa, M. (2011). Ionospheric disturbances triggered by the 11 March 2011 M9.0 Tohoku earthquake. *Journal of Geophysical Research*, *116*, A06319. https://doi.org/10.1029/2011JA016761

Liu, J. Y., Lin, C. H., Chen, Y. I., Lin, Y. C., Fang, T. W., Chen, C. H., et al. (2006). Solar flare signatures of the ionospheric GPS total electron content. *Journal of Geophysical Research*, *111*, A05308. https://doi.org/10.1029/2005JA011306

Liu, J. Y., Lin, C. H., Tsai, H. F., & Liou, Y. A. (2004). Ionospheric solar flare effects monitored by the ground-based GPS receivers: Theory and observation. *Journal of Geophysical Research*, *109*, A01307. https://doi.org/10.1029/2003JA009931

Liu, J. Y., Sun, Y. Y., Kakinami, Y., Chen, C. H., Lin, C. H., & Tsai, H. F. (2011). Bow and stern wave s triggered by the Moon's shadow boat. *Geophysical Research Letters*, *38*, L17109. https://doi.org/10.1029/2011GL048805

Liu, J. Y., Tsai, Y. B., Chen, S. W., Lee, C. P., Chen, Y. C., Yen, H. Y., et al. (2006). Giant ionospheric disturbances excited by the *M*9.3 Sumatra earthquake of 26 December 2004. *Geophysical Research Letters*, *33*, L02103. https://doi.org/10.1029/2005GL023963

Liu, J. Y., Yang, W. H., Lin, C. H., Chen, Y. I., & Lee, I. T. (2013). A statistical study on the characteristics of ionospheric storms in the equatorial ionization anomaly region: GPS-TEC observed over Taiwan. *Journal of Geophysical Research: Space Physics*, *118*, 3856–3865. https://doi.org/10.1002/jgra.50366

Mannucci, A. J., Tsurutani, B. T., Iijima, B. A., Komjathy, A., Saito, A., Gonzalez, W. D., et al. (2005). Dayside global ionospheric response to the major interplanetary events of October 29–30, 2003 "Halloween Storms". *Geophysical Research Letters*, *32*. L12S02. https://doi.org/10.1029/2004GL021467

Mendillo, M., & Forbes, J. (1978). Artificially created holes in the ionosphere. *Journal of Geophysical Research*, *83*(A1), 151–163. https://doi.org/10.1029/JA083iA01p00151

Mendillo, M., Hawkins, G. S., & Klobuchar, J. A. (1975). A sudden vanishing of the ionospheric *F* region due to the launch of Skylab. *Journal of Geophysical Research*, *80*(16), 2217–2228. https://doi.org/10.1029/JA080i016p02217

Mendillo, M., Smith, S., Coster, A., Erickson, P., Baumgardner, J., & Martinis, C. (2008). Man-made space weather. *Space Weather*, *6*. S09001. https://doi.org/10.1029/2008SW000406

Miller, S. D., Straka, W. C., Yue, J., Smith, S. M., Alexander, M. J., Hoffmann, L., et al. (2015). Upper atmospheric gravity wave details revealed in nightglow satellite imagery. *Proceedings of the National Academy of Sciences*, *112*(49), E6728–E6735. https://doi.org/10.1073/pnas.1508084112

Nakashima, Y., & Heki, K. (2014). Ionospheric hole made by the 2012 North Korean rocket observed with a dense GNSS array in Japan. *Radio Science*, *49*, 497–505. https://doi.org/10.1002/2014RS005413

Nishioka, M., Tsugawa, T., Kubota, M., & Ishii, M. (2013). Concentric waves and short-period oscillations observed in the ionosphere after the 2013 Moore EF5 tornado. *Geophysical Research Letters*, *40*, 5581–5586. https://doi.org/10.1002/2013GL057963

Noble, S. T. (1990). A large-amplitude traveling ionospheric disturbance excited by the space shuttle during launch. *Journal of Geophysical Research*, *95*(19), 037–19,044.

Ozeki, M., & Heki, K. (2010). Ionospheric holes made by ballistic missiles from North Korea detected with a Japanese dense GPS array. *Journal of Geophysical Research*, *115*, A09314. https://doi.org/10.1029/2010JA015531

Park, J., Kil, H., Stolle, C., Lühr, H., Coley, W. R., Coster, A., & Kwak, Y.-S. (2016). Daytime midlatitude plasma depletions observed by Swarm: Topside signatures of the rocket exhaust. *Geophysical Research Letters*, *43*, 1802–1809. https://doi.org/10.1002/2016GL067810

Picone, J. M., Hedin, A. E., Drob, D. P., & Aikin, A. C. (2002). NRLMSISE-00 empirical model of the atmosphere: Statistical comparisons and scientific issues. *Journal of Geophysical Research*, *107*(A12), 1468. https://doi.org/10.1029/2002JA009430

Richmond, A. D. (1978). Gravity wave generation, propagation, and dissipation in the thermosphere. *Journal of Geophysical Research*, *83*(A9), 4131–4145. https://doi.org/10.1029/JA083iA09p04131

Siskind, D. E., Stevens, M. H., Emmert, J. T., Drob, D. P., Kochenash, A. J., Russell, J. M. III, et al. (2003). Signatures of shuttle and rocket exhaust plumes in TIMED/SABER radiance data. *Geophysical Research Letters*, *30*(15), 1819. https://doi.org/10.1029/2003GL017627

Sun, Y.-Y., Liu, J.-Y., Lin, C.-H., Lin, C.-Y., Shen, M.-H., Chen, C.-H., et al. (2018). Ionospheric bow wave induced by the moon shadow ship over the continent of United States on 21 August 2017. *Geophysical Research Letters*, *45*. https://doi.org/10.1002/2017GL075926

Sun, Y.-Y., Liu, J.-Y., Lin, C.-Y., Tsai, H.-F., Chang, L. C., Chen, C.-Y., & Chen, C.-H. (2016). Ionospheric F_2 region perturbed by the 25 April 2015 Nepal earthquake. *Journal of Geophysical Research: Space Physics*, *121*, 5778–5784. https://doi.org/10.1002/2015JA022280

Tanaka, T. (1986). Low-latitude ionospheric disturbances: Results for March 22, 1979, and their general characteristics. *Geophysical Research Letters*, *13*(13), 1399–1402. https://doi.org/10.1029/GL013i013p01399

Tsai, H. F., & Liu, J. Y. (1999). Ionospheric total electron content response to solar eclipses. *Journal of Geophysical Research*, *104*(A6), 12,657–12,668. https://doi.org/10.1029/1999JA900001

Vadas, S. L., & Fritts, D. C. (2005). Thermospheric responses to gravity waves: Influences of increasing viscosity and thermal diffusivity. *Journal of Geophysical Research*, *110*, D15103. https://doi.org/10.1029/2004JD005574

Wang, T.-S. (2001). Thermophysics characterization of kerosene combustion. *Journal of Thermophysics and Heat Transfer*, *15*(2).

Yang, Y.-M., Garrison, J. L., & Lee, S.-C. (2012). Ionospheric disturbances observed coincident with the 2006 and 2009 North Korean underground nuclear tests. *Geophysical Research Letters*, *39*, L02103. https://doi.org/10.1029/2011GL050428

Yeh, K. C., & Liu, C. H. (1974). Acoustic gravity waves in the upper atmosphere. *Reviews of Geophysics*, *12*(2), 193–216. https://doi.org/10.1029/RG012i002p00193

Yue, J., Vadas, S. L., She, C.-Y., Nakamura, T., Reising, S. C., Liu, H.-L., et al. (2009). Concentric gravity waves in the mesosphere generated by deep convective plumes in the lower atmosphere near Fort Collins, Colorado. *Journal of Geophysical Research*, *114*, D06104. https://doi.org/10.1029/2008JD011244

Zhang, S.-R., Erickson, P. J., Goncharenko, L. P., Coster, A. J., Rideout, W., & Vierinen, J. (2017). Ionospheric bow waves and perturbations induced by the 21 August 2017 solar eclipse. *Geophysical Research Letters*, *44*, 12,067–12,073. https://doi.org/10.1002/2017GL076054